NACA

RESEARCH MEMORANDUM

TOTAL-PRESSURE RECOVERY OF A CIRCULAR UNDERSLUNG INLET

WITH THREE DIFFERENT NOSE SHAPES AT

A MACH NUMBER OF 1.42

By Charles F. Merlet and Howard S. Carter

Langley Aeronautical Laboratory
Langley Field, Va.
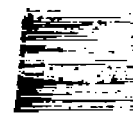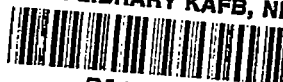
NATIONAL ADVISORY COMMITTEE
FOR AERONAUTICS

WASHINGTON
February 25, 1952

NATIONAL ADVISORY COMMITTEE FOR AERONAUTICS

RESEARCH MEMORANDUM

TOTAL-PRESSURE RECOVERY OF A CIRCULAR UNDERSLUNG INLET

WITH THREE DIFFERENT NOSE SHAPES AT

A MACH NUMBER OF 1.42

By Charles F. Merlet and Howard S. Carter

SUMMARY

A circular underslung inlet located well forward on a body of revo-
lution - modified by drooping the nose in the direction of the inlet -
was tested at a Mach number of 1.42 in a free-air jet. Three nose shapes,
one pointed and two spherical, were tested through a range of mass-flow
ratios at three different angles of attack and one angle of yaw. Total-
pressure recoveries at the inlet and after diffusion were measured and
shadowgraphs obtained for each nose shape.

Total-pressure recoveries of 0.99 were measured at the inlet for
the pointed nose, while rounding the nose produced recoveries from 2 per-
cent to 5 percent lower at 0° and 7° angles of attack. At -7° angle of
attack, the shock wave ahead of the inlet interacting with the boundary
layer thickened by cross flow resulted in separation and, consequently,
in a loss of approximately 6 percent in total-pressure recovery. The
yaw tests yielded total-pressure recoveries at the inlet essentially the
same as those at 0° angle of attack for all three nose shapes.

At the angles tested other than -7° angle of attack, the circular
shape of the inlet, plus the $\frac{1}{8}$-inch gap between the inlet lip and the
body aided in bypassing the boundary layer. At low mass flows, although
considerable separation was evident ahead of the inlet, none of the
separated flow entered. At high mass flows, much less separation was
evident but a negligible amount did enter.

The subsonic diffuser and bend losses amounted to a maximum of
4 percent of the inlet total pressure when diffusing from sonic Mach
number at the minimum area station, except when separated flow entered
the inlet.

INTRODUCTION

Since the nose of an airplane may not be available for an air inlet because of the use of the nose for radar or other equipment, information is needed concerning the performance of inlets located elsewhere. In view of this need, a circular underslung inlet model has been constructed for flight testing by the Pilotless Aircraft Research Division of the Langley Aeronautical Laboratory. This paper presents the results of the preflight tests of this model.

The particular scoop inlet selected was located well forward on the parabolic body of revolution reported in reference 1. The forward portion of the body was modified by tilting the nose in the direction of the scoop in an effort to alleviate the amount of turning necessary at the inlet for the entering air. An inlet of circular cross section, having the same area and internal lip shape as the nose inlet reported in reference 2, was used. It was felt that the circular shape provided a structurally strong configuration around which the boundary layer could be easily passed.

In keeping with the idea that the nose may be used for radar equipment, two alternate nose shapes were also selected for testing. Spherical shapes were used as being acceptable from a radar standpoint. The two spherically shaped noses varied in size, one having a diameter 30 percent of the maximum body diameter and the other with a diameter 40 percent of the maximum body diameter.

Total-pressure recoveries and shadowgraphs for all three nose shapes were obtained at three angles of attack and one angle of yaw in a Mach number 1.42 free-air jet.

SYMBOLS

A   area

D   diameter

H   total pressure

M   Mach number

d   vertical distance, measured from the uppermost point of the inner wall at the first minimum-area station (see fig. 1(c))

m/m_0 ratio of the mass flow through duct to the mass flow
            through a free-stream tube of area equal to the inlet
            area

p static pressure

s distance along vertical diameter, measured from the upper-
            most point of the throat (see fig. 1(b))

α angle of attack

ψ angle of yaw

γ ratio of specific heats; 1.40 for air

Subscripts:

o   free stream, at nozzle exit

i   inlet station at leading edge of the lips, station 7.90

1   first minimum-area station, station 8.32

t   throat station, station 43.25

A bar over a symbol indicates an average value (see section entitled
"Method of Analysis").

MODEL

The model (fig. 1(a)) consisted of a basic parabolic body, made of
wood, to which a circular underslung inlet was added. The inlet and
ducting were made of aluminum. The body coordinates rearward of sta-
tion 10 are the same as those of the parabolic body reported in refer-
ence 1. At station 8, the center line of the nose was canted downward
about 7° with respect to the center line of the fuselage.

The inlet (fig. 1(b)) was located rearward of the pointed nose about
9 percent of the body length. A circular cross section was selected as
a shape around which the boundary layer could be passed conveniently,
since the circular inlet was close to the body in only a very small region.
A $\frac{1}{8}$ -inch gap between the inlet and the body was used to aid further in
bypassing the boundary layer. The inlet lip shape (fig. 1(c)), inter-
nally the same as that used on the nose inlet of reference 2, was rounded

to provide a bellmouthed shape for subsonic operations. The resulting minimum area, 0.42 inch rearward of the leading edge of the lip, was 88 percent of the inlet area.

The initial total diffuser angle of 2.5° was maintained to station 9.96 where the duct area was 1.10 times the minimum area. Transition was then made to a 4° total-angle diffuser. The over-all diffuser area ratio between stations 8.4 and 27.2 was 2.3 to 1.0. Following the diffuser was a constant-area compound offset bend, with a radius of curvature four times the diameter of the section. Rearward of the bend the duct was contracted to 0.75 times the maximum diffuser area to form a throat, which was instrumented to measure air flow.

Four vane-type shutters, installed rearward of the throat, and rotated at a constant speed by an electric motor during the tests, varied the air flow from a maximum to a minimum in about 13 seconds for most of the tests. Several runs, made with the shutters stationary, showed that the rotation speed was slow enough to yield steady-state results.

Three nose shapes were tested (fig. 1(b)). The first, described above, will be referred to as the pointed nose. The second, made by cutting the original pointed nose to form a 1.5-inch-radius spherical nose shape with the forward tip about 3.5 inches ahead of the inlet, will be referred to as the 1.5-inch-radius nose. The third, made by cutting the original pointed nose to form a 2-inch-radius spherical nose shape with the forward tip about 1.7 inches ahead of the inlet, will be referred to as the 2-inch-radius nose. The spherical nose shapes were selected to simulate configurations acceptable with regard to requirements for nose radar installations.

INSTRUMENTATION

Total pressures at the inlet were measured at station 8.4 by six total-pressure tubes placed circumferentially around the inlet as shown in figure 1(c). Two diametrically opposite wall orifices, also shown in figure 1(c), measured the inlet static pressure at the same station.

Total pressures at the throat were measured at station 43.2 by a seven-tube rake. Measuring from the top duct wall, the tubes were located at 0.03, 0.15, 0.30, 0.50, 0.70, 0.84, and 0.95 diameter on a vertical diameter across the throat. Static pressure at the same station was measured by six wall orifices equally spaced around the duct and manifolded together. The free-stream total pressure and static pressure were also measured.

Pressures were recorded by mechanical optical pressure recorders and electrical pressure recorders of the strain-gage type. Time histories of the pressures were obtained on film. Shadowgraphs were obtained for all tests. For the tests made with the model at -7° angle of yaw, the shadowgraph camera was also yawed with respect to the free stream, so that the plane of the camera was parallel to the plane of symmetry of the model.

TESTS

The tests were made in the preflight jet of the Pilotless Aircraft Research Station at Wallops Island, Va. (reference 3). A 12-inch square nozzle with an exit Mach number of 1.42 was used. The tip of the model was placed about 1.5 inches downstream of the plane of the nozzle for most of the tests. Figure 2 shows a photograph of the model in this position in the jet. The model was placed upside down for ease of instrumentation.

The three nose shapes were tested at 0°, 7°, and -7° angles of attack with 0° angle of yaw, and at -7° angle of yaw with 0° angle of attack. The fuselage reference line for specifying the angles of attack and yaw is labeled in figure 1(b).

Hereafter the only angle mentioned shall be the angle which was varied from 0°, for example, 7° angle of attack with 0° angle of yaw shall be referred to as 7°α. Tests at 0° angle of attack with 0° angle of yaw shall be referred to as tests at 0°α.

The Reynolds number for all tests was approximately 15×10^6 per foot.

METHOD OF ANALYSIS

Measurements made at the throat station were used to compute the mass-flow ratios and total-pressure recoveries after diffusion by numerical integration of the total pressure and Mach number profiles obtained from the rake measurements. The two equations used were

$$\frac{m}{m_o} = \frac{\int_{A_t} p_t M_t \left(1 + \frac{\gamma - 1}{2} M_t^2\right)^{1/2} dA}{p_o M_o \left(1 + \frac{\gamma - 1}{2} M_o^2\right)^{1/2} A_1} \qquad (1)$$

$$\overline{H}_t = \frac{1}{A_t} \int_{A_t} H_t \, dA \qquad (2)$$

Computation of $\overline{H}_t/H_o$ weighted on a mass-flow-ratio basis for several cases yielded results that agreed, within the experimental accuracy of ±0.004, with the values weighted on area as obtained from equation (2).

In obtaining $\overline{H}_1$, it was assumed that there was no variation in total pressure horizontally across the first minimum-area station as data obtained from tubes B and C (see fig. 1(c) for tube locations) were equal. A total-pressure distribution was then plotted along the vertical diameter and $\overline{H}_1$ was obtained by numerical integration, weighted on area, using equation (2) with appropriate changes in the subscript. Because of the proximity of the first minimum-area station to the inlet, the average total-pressure recovery at the inlet $\overline{H}_i$ was assumed equal to $\overline{H}_1$. Again, weighting the total-pressure recovery at the inlet on a mass-flow-ratio basis resulted in differences within the experimental accuracy of ±0.002 when compared to the values weighted by area.

Comparison of the static-pressure measurements obtained from the two diametrically opposite static-pressure orifices indicated a static-pressure gradient across the first minimum-area station. In computation of mass-flow ratios at this station, this variation was assumed to be linear. Equation (1), with appropriate changes in the subscripts, was used to compute mass-flow ratios. Agreement between the mass-flow ratios computed at the first minimum-area station and those computed at the throat were within 0.02 at $\frac{m}{m_o} = 0.80$ and 0.05 at a $\frac{m}{m_o} = 0.40$.

RESULTS AND DISCUSSION

Pointed Nose

Shadowgraphs of the flow with the pointed nose installed are shown in figures 3 to 7, for $0^\circ\alpha$, $7^\circ\alpha$, $-7^\circ\psi$, and $-7^\circ\alpha$. The Mach waves seen entering the pictures from the upper and lower left side were caused by slight surface irregularities at the nozzle exit. Shadowgraphs of the model in yaw (fig. 5), taken with the camera in a plane parallel to the yawed model, showed a series of Mach waves extending across the nozzle. It is believed many of them did not actually contact the model. To check the effect of these Mach waves on the entering air flow, tests were made with the tip of the model about 2.5 inches in the nozzle. These Mach waves then appeared to intersect the strong shock ahead of the inlet (fig. 3(a)). The shadowgraph showed that separation occurred at the same station and pressure measurements showed no change for either location of the model, indicating that the effect of the Mach waves can be neglected in further analysis of the data.

At all angles, the shadowgraphs show a conical shock from the nose followed by a strong shock ahead of the inlet. The strong shock moved upstream with decreasing mass flow.

At $0^\circ\alpha$, figure 3 shows that as mass-flow ratio decreases the strong shock became a lambda shock. Although a lambda shock often denotes laminar separation, in each of the present tests the flow ahead of the separation point is believed to have been turbulent; this conclusion is based partly on the presence of the weak shocks along the body which indicate sufficient roughness to cause a turbulent boundary layer. As mass flow decreased, the boundary layer thickened and then separated in the region of the foreleg of the lambda shock. At high mass-flow ratio (fig. 3(b)), a portion of the thickened boundary layer appears to enter the inlet, but at lower mass-flow ratio, despite increased separation, it was not carried into the inlet, as indicated in figure 3(d). The cross flow, existing over the nose portion at $0^\circ\alpha$ because the nose was tilted downward, caused a thick boundary layer on the side of the body ahead of the inlet. Interaction of the strong shock preceding the inlet with this thickened boundary layer resulted in the separation on the nose.

At $7^\circ\alpha$ (fig. 4) and at $-7^\circ\psi$ (fig. 5), the boundary layer was thinner than it was at $0^\circ\alpha$ throughout the mass-flow range. There was no separation at $7^\circ\alpha$, and only slight separation at $-7^\circ\psi$.

At $-7^\circ\alpha$ (fig. 6), as mass flow was decreased, a lambda shock appeared and boundary-layer separation took place near the foreleg of this

lambda shock. The region of separated flow became larger with decreases in mass-flow ratio until at a mass-flow ratio of 0.44 (fig. 6(c)) it extended completely across the inlet.

The flow became unstable at minimum mass flow, as illustrated by a time sequence of shadowgraphs in figure 7. This flow instability appears to be similar to the buzz phenomenon experienced by other external compression inlets at low mass-flow ratios.

Figure 8 shows the total-pressure recovery measured with inlet tube A (see fig. 1(c) for tube location) plotted against mass-flow ratio for all angles tested. As shown by the shadowgraph, boundary layer entered the inlet at $0^{\circ}\alpha$ at the high mass-flow ratios. Below $\frac{m}{m_O} = 0.6$, tube A no longer indicated large losses, hence the boundary layer must have become reattached ahead of the inlet or passed around the inlet. Tube A was the only inlet tube indicating large losses at this angle of attack. At $7^{\circ}\alpha$ and $-7^{\circ}\psi$, the boundary layer apparently never entered the inlet. At $-7^{\circ}\alpha$, however, tube A measured low recoveries throughout the mass-flow range, as might be expected from the extensive separation evident on the shadowgraphs in figures 6 and 7.

The average total-pressure recoveries at the inlet and in the throat obtained with the pointed nose installed are presented in figure 9 as a function of mass-flow ratio. For $0^{\circ}\alpha$, $7^{\circ}\alpha$, and $-7^{\circ}\psi$, the total-pressure recovery measured at the inlet is shown in figure 9(a). This recovery remained relatively constant at about 0.99 for most mass-flow ratios. It appears then that the effect of entering boundary layer at $0^{\circ}\alpha$ is slight, indicating the region of low-energy air was small. Because the conical shock at the tip of the model with very little total-pressure loss reduced the Mach number at which the strong shock at the inlet occurred, the recovery at the inlet was nearly 4 percent higher than the free-stream normal-shock recovery.

At $-7^{\circ}\alpha$, the separation that occurred ahead of the inlet made it impractical to determine an average inlet total-pressure recovery. Therefore, the average total-pressure recovery at the throat is presented for this angle of attack in figure 9(b). The average throat recovery measured at $0^{\circ}\alpha$, which is typical of the recovery obtained at $7^{\circ}\alpha$ and $-7^{\circ}\psi$ also, is included to indicate the magnitude of the losses caused by separation.

1.5-Inch-Radius Nose

Shadowgraphs of the flow with the 1.5-inch-radius nose are presented in figures 10 to 13 for $0°\alpha$, $7°\alpha$, $-7°\psi$, and $-7°\alpha$. For all tests, there was a strong bow wave ahead of the model and a lambda shock ahead of the inlet. The bow wave was relatively unchanged as mass-flow ratio varied, but the lambda shock moved forward as mass-flow ratio decreased.

At $0°\alpha$ (fig. 10), separation occurred at the foreleg of the lambda shock. The separated region thickened as mass-flow ratio decreased. At $7°\alpha$ (fig. 11) and $-7°\psi$ (fig. 12), the boundary layer was thinner at all mass-flow ratios than it was at $0°\alpha$.

At $-7°\alpha$ (fig. 13), the boundary-layer separation, occurring in the region of the foreleg of the lambda shock, became increasingly greater as mass flow decreased, in a manner similar to the behavior of the pointed nose at this angle of attack. This nose shape also exhibited flow instability at minimum mass-flow ratio.

Figure 14 presents the total-pressure recovery of inlet tube A as a function of mass-flow ratio for the 1.5-inch-radius nose. As with the pointed nose, no low-energy air entered the inlet at $7°\alpha$ and $-7°\psi$. At $0°\alpha$, the recovery of tube A increased as mass-flow ratio decreased until at minimum mass-flow ratio there was no boundary layer on entering the inlet. At $-7°\alpha$, tube A showed the presence of separated flow throughout the mass-flow range.

The average total-pressure recovery at the inlet for the 1.5-inch-radius nose is presented in figure 15(a) as a function of mass-flow ratio for $0°\alpha$, $7°\alpha$, and $-7°\psi$. In all three cases, the recovery decreased with increasing mass-flow ratio. Since the bow wave remained relatively unchanged with changing mass-flow ratio, the losses across it were unchanged. The flow, subsonic behind the bow wave in the immediate region of the nose, expanded around the nose section and attained increasing supersonic velocities along the body. Since decreasing the mass flow caused the strong shock to move upstream, the shock occurred at a lower Mach number, thus decreasing the losses across it.

The higher recovery at $7°\alpha$ over that measured at $0°\alpha$ is primarily due to the change in velocity ahead of the inlet caused by the change in angle of attack. At $7°\alpha$, the flow on the inlet side of the nose did not expand to as high a Mach number as it did at $0°\alpha$. Hence the loss across the strong shock preceding the inlet, which must then have occurred at a lower Mach number, was lower. Since the bow wave was relatively unchanged, the over-all recovery was higher. The absence of boundary layer in the inlet at $7°\alpha$ also caused the recovery to be somewhat higher at the higher mass-flow ratios.

Since separation at $-7^\circ\alpha$ again made it impractical to obtain an average inlet total-pressure recovery, figure 15(b) presents the average total-pressure recovery at the throat for this angle. Again, the recovery at $0^\circ\alpha$ at the throat is included as representative of the throat recoveries measured at the other angles. The difference between the two curves indicates losses of approximately 6 percent at all mass-flow ratios.

2-Inch-Radius Nose

Shadowgraphs of the flow with the 2-inch-radius nose are presented in figures 16 to 18 for $0^\circ\alpha$, $7^\circ\alpha$, and $-7^\circ\alpha$, respectively. The shadowgraphs for $-7^\circ\psi$ were identical with those at $0^\circ\alpha$.

At all angles tested, the model was preceded by a strong bow wave. A strong shock ahead of the inlet was present only at $-7^\circ\alpha$ for $\frac{m}{m_0} > 0.9$. In all other cases the flow was subsonic from the bow wave to the inlet except for a small region of supersonic flow indicated by a short normal shock at the surface at higher mass flows. As mass flow decreased, the bow wave ahead of the inlet became more normal.

At $0^\circ\alpha$ (fig. 16) and at $-7^\circ\psi$ separation occurred on the nose just ahead of the inlet at high mass-flow ratio. As mass-flow ratio decreased, however, the boundary layer appears to no longer have entered the inlet. At $7^\circ\alpha$ (fig. 17) the shadowgraph indicates that the boundary layer did not enter the inlet even at high mass-flow ratios.

At $-7^\circ\alpha$ (fig. 18) with $\frac{m}{m_0} > 0.9$, a strong shock occurred ahead of the inlet. Boundary-layer separation occurred, with some of the separated flow entering the inlet. At lower mass-flow ratios, however, the strong shock ahead of the inlet disappeared and the boundary layer appeared no longer to enter the inlet.

Figure 19 shows the total-pressure recovery measured by tube A at the inlet with the 2-inch-radius nose. With this nose shape, tube A indicated the presence of some lower-energy air for $\frac{m}{m_0} > 0.8$ at $0^\circ\alpha$ and $-7^\circ\psi$. At $7^\circ\alpha$, and for $\frac{m}{m_0} < 0.8$ at $0^\circ\alpha$ and $-7^\circ\psi$, there was no boundary layer entering the inlet. At $-7^\circ\alpha$, however, tube A recorded large losses at high mass-flow ratios. The recovery of tube A increased rapidly with decreasing mass-flow ratio, only to decrease slightly, however, below a mass-flow ratio of 0.6.

Figure 20 presents the average total-pressure recovery measured for the 2-inch-radius nose plotted against mass-flow ratio. At the inlet (fig. 20(a)), the recovery generally decreased with decreasing mass flow, as a result of the bow wave becoming more normal as mass flow decreased. The recoveries for $0^\circ\alpha$ and $-7^\circ\psi$ were identical, and slightly higher than the recovery at $7^\circ\alpha$, throughout most of the mass-flow range. The inlet recovery for $-7^\circ\alpha$ was higher than the recovery at $0^\circ\alpha$ up to a mass-flow ratio of about 0.8; however, the inlet recovery at $-7^\circ\alpha$ began to decrease as mass flow increased above a mass-flow ratio of 0.7 due to the losses caused by separation.

Figure 20(b) shows the recovery at the throat for $0^\circ\alpha$ and $-7^\circ\alpha$ plotted against mass-flow ratio for the 2-inch-radius nose. Both curves show decreased recovery at high mass-flow ratios due to the presence of separated flow in the inlet as indicated by tube A in figure 19. Since the separation was more severe at $-7^\circ\alpha$, the recovery at this angle was less.

Comparison of the Three Nose Shapes

The data presented in figures 9, 15, and 20 are replotted in figure 21 to show the effect of nose shape on the total-pressure recovery. Figures 21(a), 21(b), and 21(c) present the inlet recoveries at $0^\circ\alpha$, $7^\circ\alpha$, and $-7^\circ\psi$, respectively. Because the total-pressure losses through the conical shock with the pointed nose were smaller than the total-pressure losses through the bow wave ahead of either round nose, the pointed nose had better recovery at the inlet at all mass-flow ratios.

In comparing the two round noses, it can be seen that the 2-inch nose had increasingly better recovery than the 1.5-inch round nose as the mass-flow ratio increased beyond 0.68 and 0.72 at $0^\circ\alpha$ and $-7^\circ\psi$, respectively. Below these mass-flow ratios the 1.5-inch nose became increasingly better. At $7^\circ\alpha$, the two rounded noses had the same recovery at maximum mass flow. As mass flow decreased, the 1.5-inch nose again became increasingly better. The minimum recovery measured with either round nose, however, was only about 1 percent lower than the free-stream normal shock recovery of 0.953 and generally the recoveries of both round noses, at these angles, were higher than the recovery through a normal shock.

Figure 21(d) shows the total-pressure recovery at the throat for the three noses at $-7^\circ\alpha$. Above $\frac{m}{m_0} = 0.6$, the pointed nose had the best recovery. Below 0.6 mass-flow ratio, the 2-inch-radius nose was the best.

It should be remembered that the losses due to separation for the pointed nose, as indicated in figure 9(b), increased at $\frac{m}{m_o} < 0.70$, while the 2-inch-radius nose had little or no apparent separation losses below a mass-flow ratio of 0.75 (fig. 20(b)). At $-7^o\alpha$, the total-pressure recovery for the 1.5-inch-radius nose was about 0.05 less than that for the 2-inch-radius nose at all mass flows, since the 1.5-inch-radius nose suffered from separation losses throughout the mass-flow range, as shown in figure 15(b).

The Diffuser-Bend Combination

Typical total-pressure distributions measured at the inlet at $0^o\alpha$ for high mass-flow ratios are shown in figure 22 for the three nose shapes tested. The presence of the entering boundary layer at the top of the duct at these mass flows is evident.

Figure 23 presents the total-pressure distributions at the throat at the same mass-flow ratios as the inlet curves presented in the previous figure. The asymmetric profile, with a higher pressure region on the bottom of the duct, occurred at all mass flows.

The total-pressure recovery of the diffuser-bend combination $\overline{H}_t/\overline{H}_1$ plotted against mass-flow ratio is shown in figure 24. The solid curve, faired through the points of measured diffuser-bend recovery at $0^o\alpha$, $7^o\alpha$, and $-7^o\psi$ for the pointed nose and at $0^o\alpha$ for both round noses, presents the diffuser-bend recovery measured when the effects of boundary layer at the inlet were relatively small. The diffuser-bend recovery decreased with increasing mass flow to a minimum value of 0.962 at the maximum mass-flow ratio of 0.95. The recovery was unaffected by the change in angle of attack or yaw, or by the change in nose shape, as long as the inlet was relatively free from separation.

The dashed curve presents the total-pressure recoveries at $-7^o\alpha$ with the 2-inch-radius nose installed and indicates the effect of separation on the diffuser-bend performance. Above a mass-flow ratio of 0.75, where the separation rapidly became greater, the diffuser-bend recovery began to decrease more rapidly than it did without separation. Thus separation not only reduced the recovery at the inlet but it also impaired the efficiency of the diffuser-bend combination.

The diffuser-bend recoveries measured at $0^o\alpha$, $7^o\alpha$, and $-7^o\psi$ for the pointed nose and at $0^o\alpha$ for both round noses are replotted in figure 25 against the average Mach number at the entrance to the diffuser. This average Mach number was computed from the total-pressure distribution

at the first minimum-area station. Also shown is the measured diffuser recovery from reference 2. The diffuser of reference 2 had a 2.5° conical diffuser angle to an area 1.2 times the minimum area at the diffuser entrance, followed by a transition to a 3.5° total angle diffuser, with an over-all area ratio of 2 to 1. Since this diffuser was used in conjunction with a nose inlet, it was not followed by a compound offset bend.

As the average entrance Mach number increased, the diffuser-bend combination of the present tests showed increasingly more losses until, at an entrance Mach number of 1.0, it had a recovery of 0.962, compared to 0.979 for the diffuser of reference 2. This lower recovery may be due to the losses associated with the compound offset bend used in the present tests.

CONCLUSIONS

Results of total-pressure measurements and shadowgraphs of preflight-jet tests of a circular underslung inlet located near the nose, at a free-stream Mach number of 1.42, indicated the following conclusions:

1. At 0° angle of attack, total-pressure recoveries at the inlet for the pointed nose attained values of 0.99, nearly 4 percent higher than the recovery that would have been obtained through a free-stream normal shock.

2. At 0° angle of attack and maximum mass-flow ratio, the 1.5-inch-radius nose and the 2-inch-radius nose had total-pressure recoveries at the inlet of 0.94 and 0.97, respectively.

3. At 7° angle of attack, the total-pressure recoveries at the inlet for both the pointed nose and the 2-inch-radius nose were approximately the same as at 0° angle of attack, while the recovery of the 1.5-inch-radius nose was increased over 2 percent at maximum mass flow.

4. At -7° angle of attack, interaction of the boundary layer, thickened by cross flow, with the strong shock ahead of the inlet resulted in separation and consequent losses of about 6 percent in recovery.

5. At -7° angle of yaw, the total-pressure recoveries at the inlet for all three nose shapes were essentially the same as at 0° angle of attack.

6. At the angles tested other than -7° angle of attack, the circular shape of the inlet and the $\frac{1}{8}$-inch gap between the inlet lip and the body

allowed only a negligible amount of boundary-layer air to enter the inlet at high mass flows. At low mass flows, despite considerable separation ahead of the inlet, none of the boundary layer entered.

7. The subsonic diffuser and bend losses amounted to a maximum of 4 percent of the inlet total pressure when diffusing from sonic Mach number at the inlet minimum area station, except when separated flow entered the inlet.

Langley Aeronautical Laboratory
    National Advisory Committee for Aeronautics
        Langley Field, Va.

REFERENCES

1. Sears, Richard I., and Merlet, C. F.: Flight Determination of the Drag and Pressure Recovery of an NACA 1-40-250 Nose Inlet at Mach Numbers from 0.9 to 1.8. NACA RM L50L18, 1951.

2. Sears, Richard I., and Merlet, C. F.: Flight Determination of Drag and Pressure Recovery of a Nose Inlet of Parabolic Profile at Mach Numbers from 0.8 to 1.7. NACA RM L51E02, 1951.

3. Faget, Maxime A., Watson, Raymond S., and Bartlett, Walter A., Jr.: Free-Jet Tests of a 6.5-Inch-Diameter Ram-Jet Engine at Mach Numbers of 1.81 and 2.00. NACA RM L50L06, 1951.
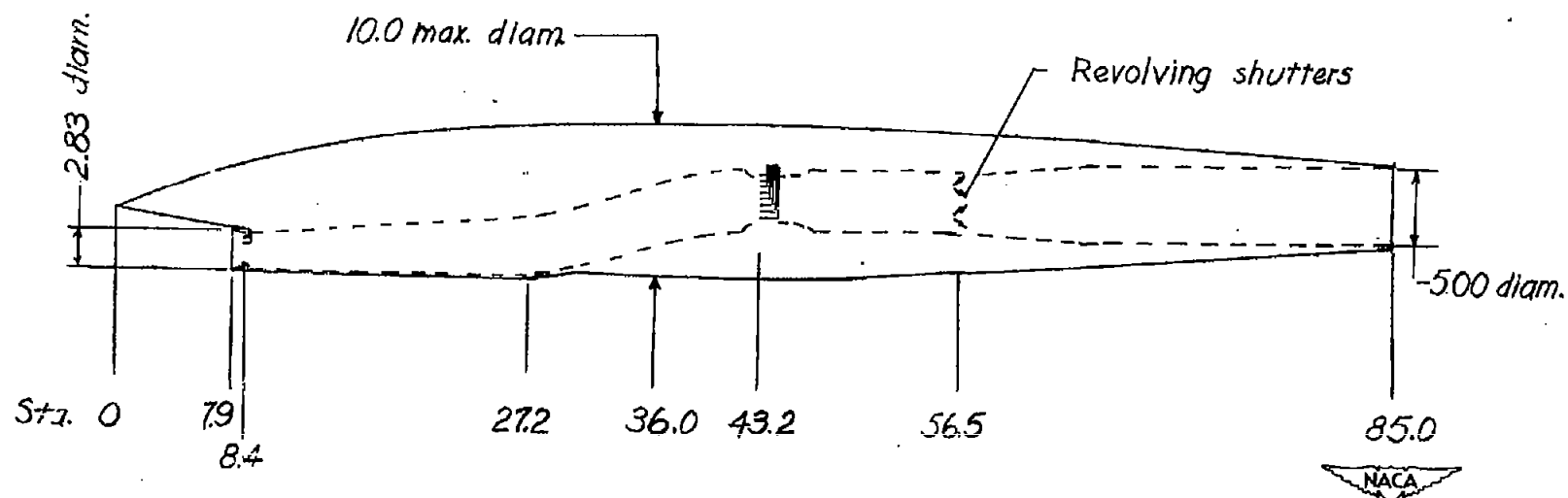
(a) General arrangement of the model.

Figure 1.- Drawings of the model. All dimensions are in inches.

Nose coordinates	
Sta.	Rad.
0	0
2.67	.72
5.33	1.39
8.00	2.00
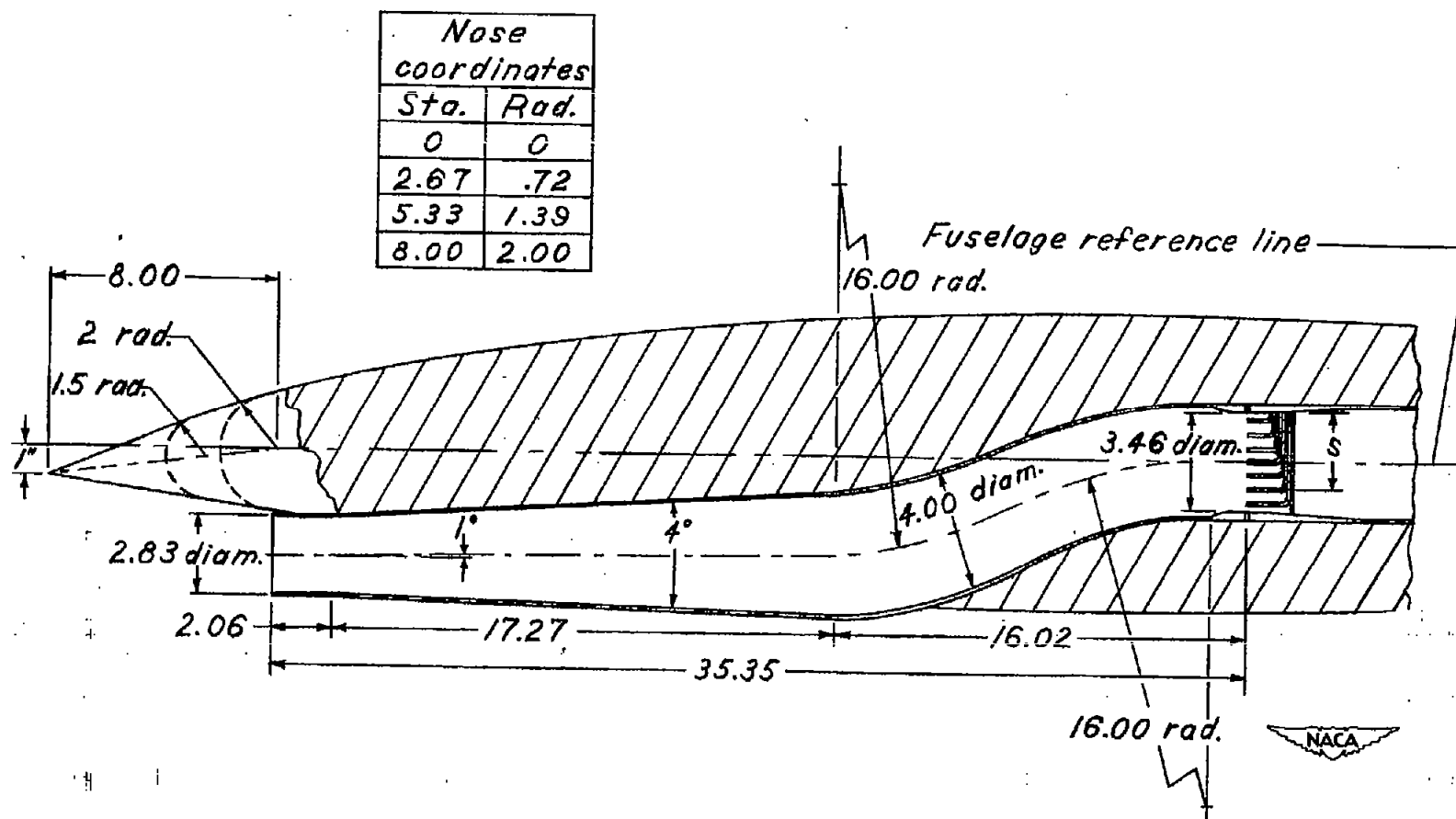
(b) Forward duct and body detail.

Figure 1.- Continued.

Tube A

$\frac{1}{16}$

$\frac{3}{8}$

Tube C

2.65 min. diam.

d

Tube B

Tube D

Tube F

$20°$

$\frac{1}{8}$

Tube E

Static-pressure tube

Section A-A

Lip coordinates		
X	Y₁	Y₂
0	0	0
.018	.021	.017
.035	.032	.022
.070	.047	.027
.105	.057	.031
.140	.065	.033
.210	.077	.036
.280	.084	.037
.420	.088	.037
.560	.085	.037

A

See detail a

$\frac{1}{8}$

2.5°

4°

1°

$\frac{1}{2}$

2.06

A

Station 9.96

$-Y_2$

Y_1

2.83 diam.

X

.560 (ref.)

Tangent point

1.25°

Detail a

NACA

(c) Details of the inlet.

Figure 1.- Concluded.
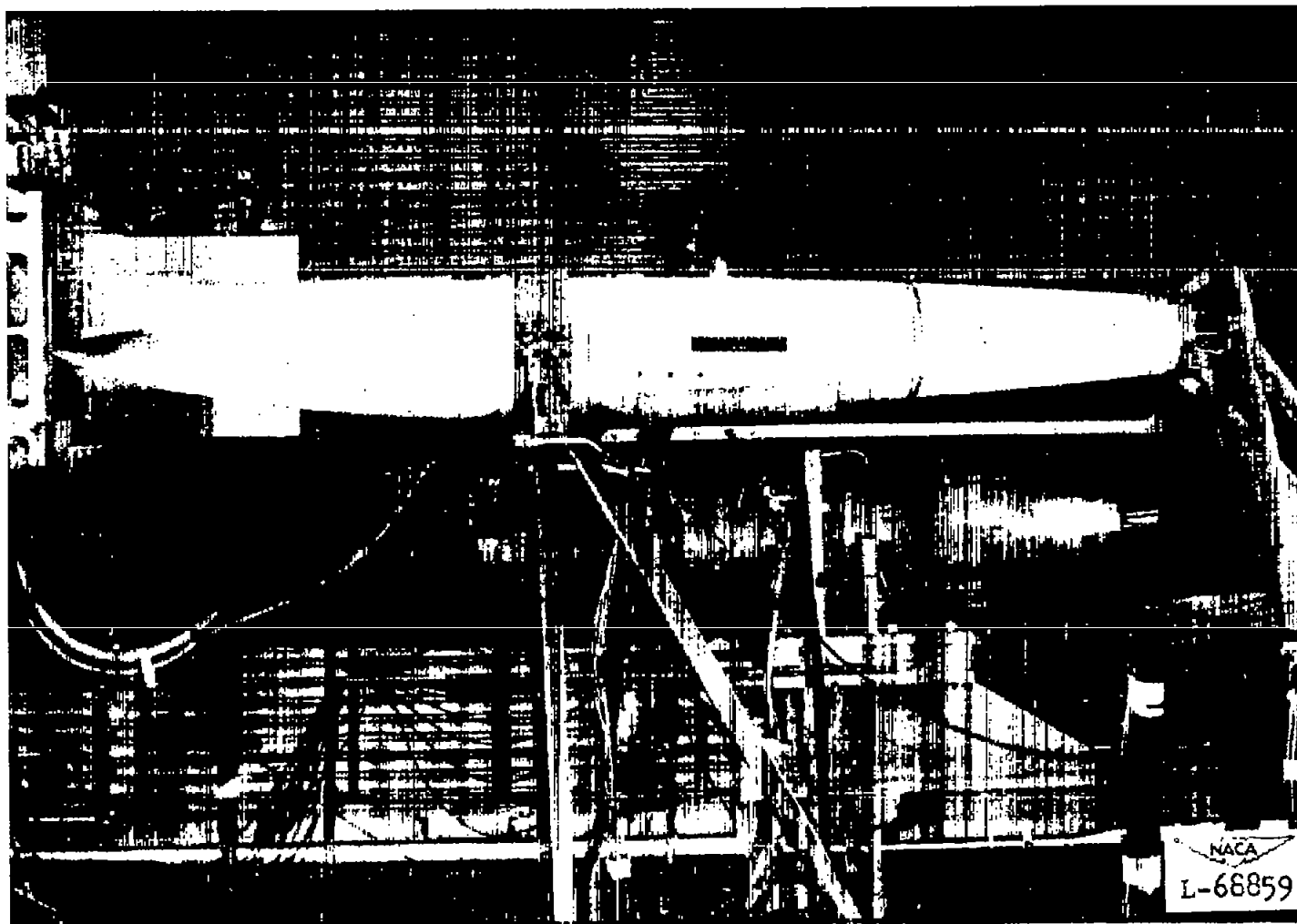
Figure 2.- Photograph of the model in the preflight jet of the Pilotless
Aircraft Research Station at Wallops Island, Va.
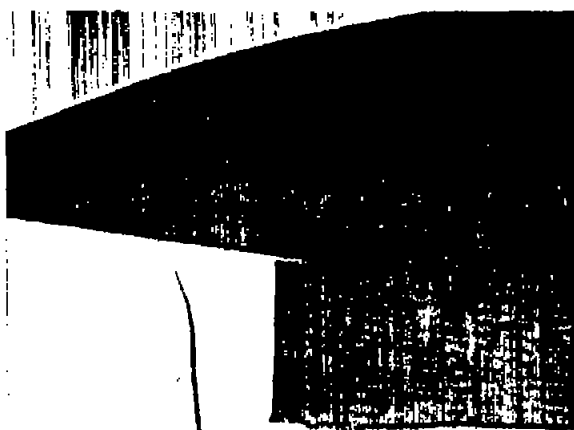
(a) $\frac{m}{m_0} = 0.70.$

(b) $\frac{m}{m_0} = 0.96.$
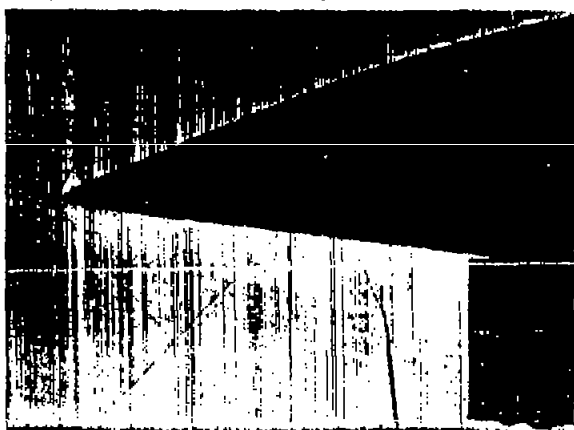
(c) $\frac{m}{m_0} = 0.70.$
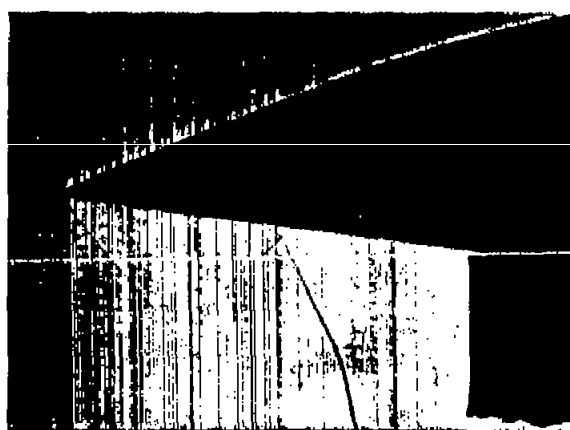
(d) $\frac{m}{m_0} = 0.31.$

L-70833

Figure 3.— Shadowgraphs of the flow with the pointed nose. $\alpha = 0^{\circ}$; $\psi = 0^{\circ}$.
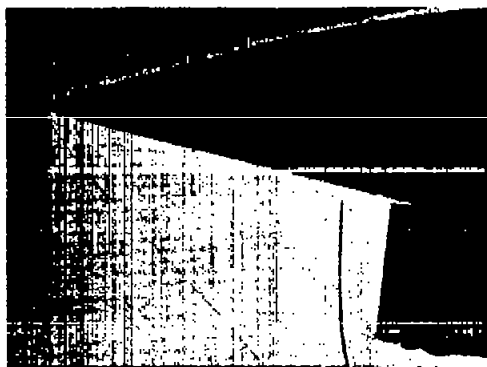
(a) $\frac{m}{m_0} = 0.97.$
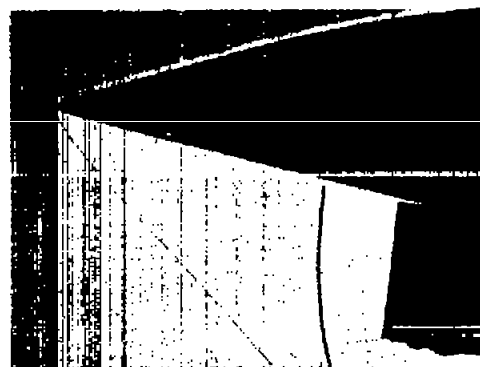
(b) $\frac{m}{m_0} = 0.63.$

L-70834

Figure 4.- Shadowgraphs of the flow with the pointed nose. $\alpha = 7^0$; $\psi = 0^0$.
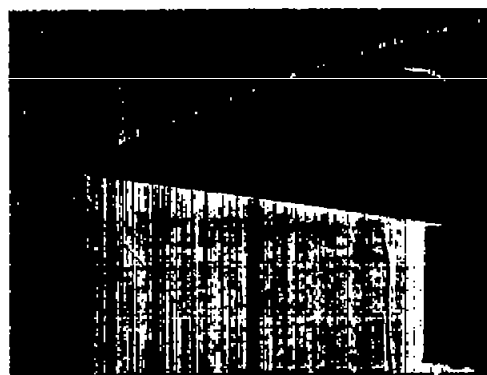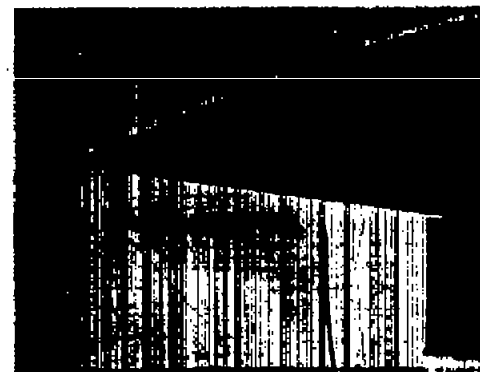
(a) $\frac{m}{m_0} = 0.96.$

(b) $\frac{m}{m_0} = 0.40.$

L-70835

Figure 5.- Shadowgraphs of the flow with the pointed nose. $\alpha = 0^0$; $\psi = -7^0$.

(a) $\frac{m}{m_0} = 0.92.$
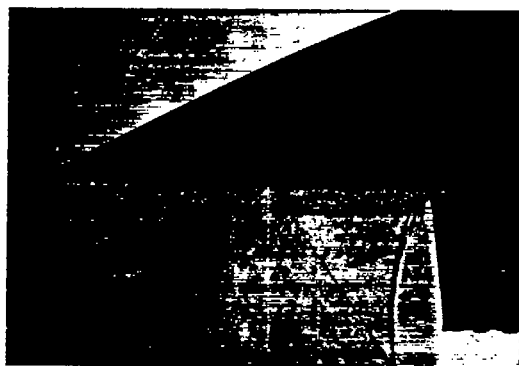
(b) $\frac{m}{m_0} = 0.88.$
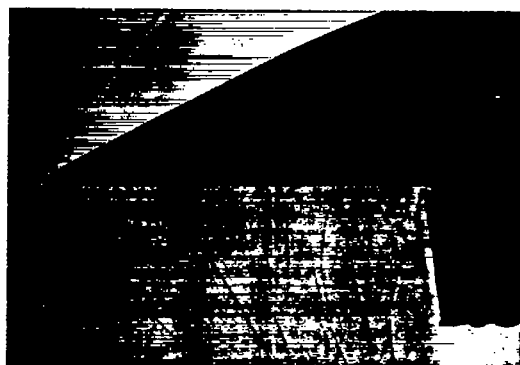
(c) $\frac{m}{m_0} = 0.44.$

L-70836

Figure 6.- Shadowgraphs of the flow with the pointed nose. $\alpha = -7°;$ $\psi = 0°.$
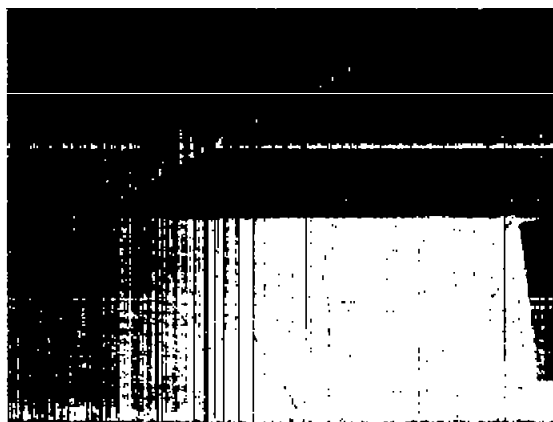
(a) Time, 0 sec.
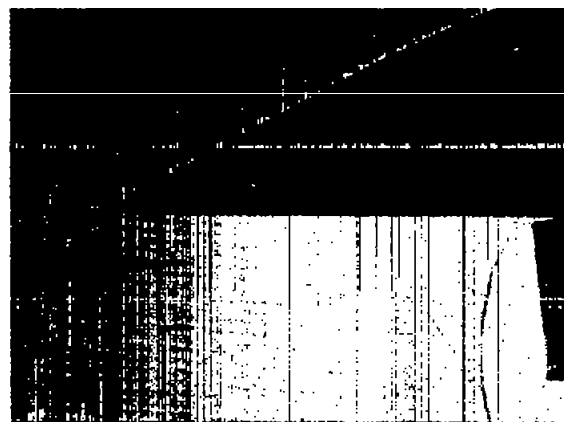
(b) Time, 0.5 sec.
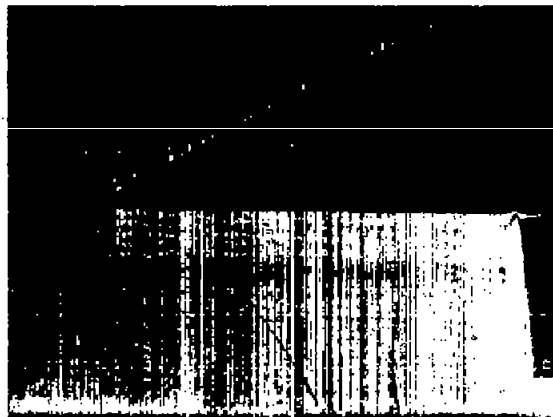
(c) Time, 2.0 sec.
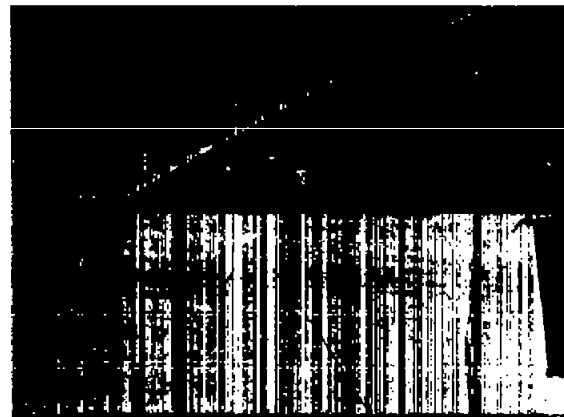
(d) Time, 2.5 sec.

Figure 7.- Shadowgraphs of the flow with the pointed nose showing flow instability at minimum mass flows. $\alpha = -7^{\circ}$; $\psi = 0^{\circ}$.

L-70837
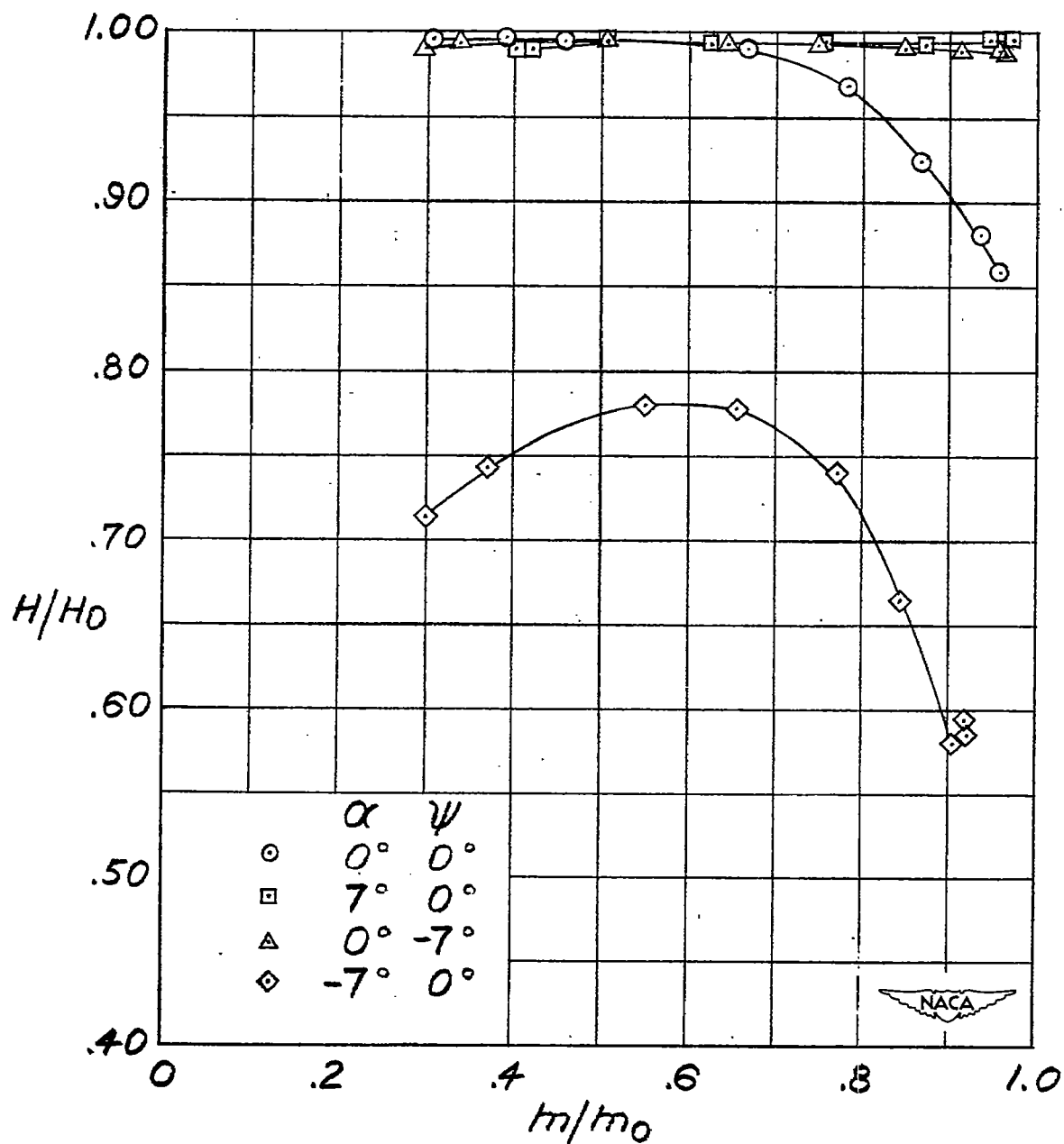
Figure 8.- Total-pressure recovery of inlet tube A with the pointed nose installed.
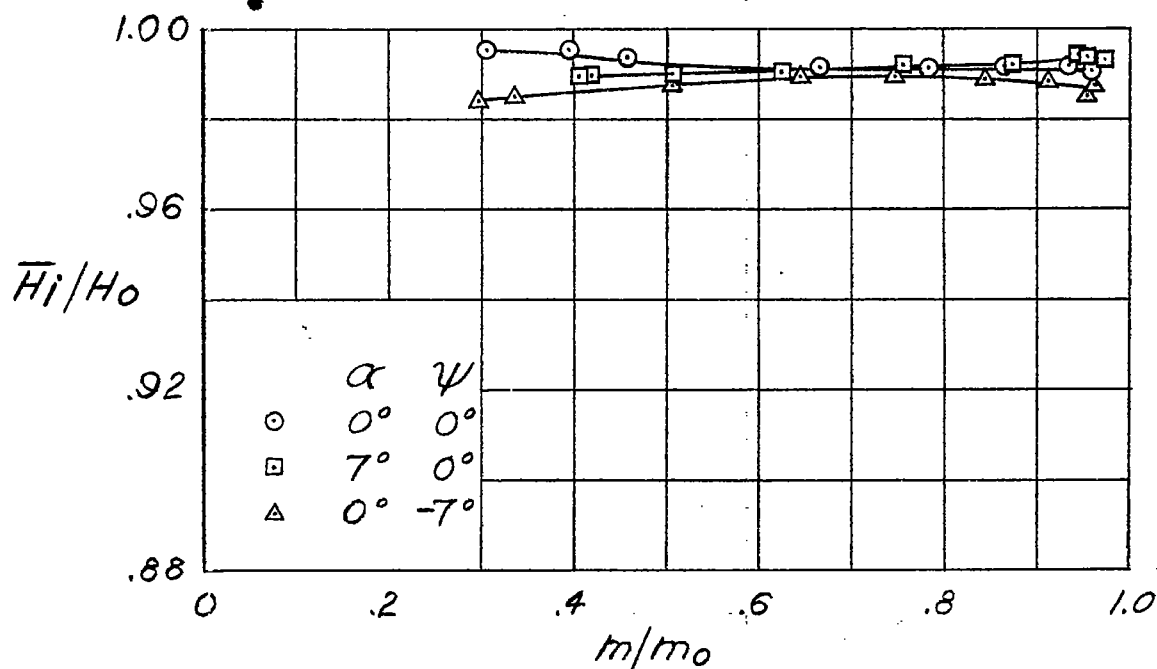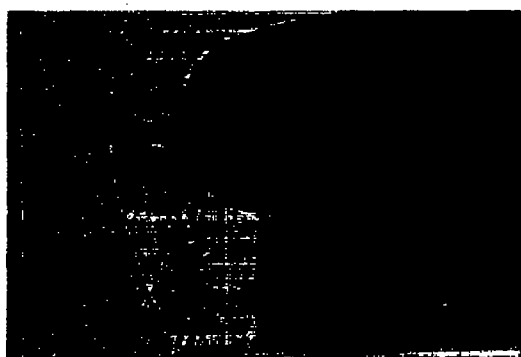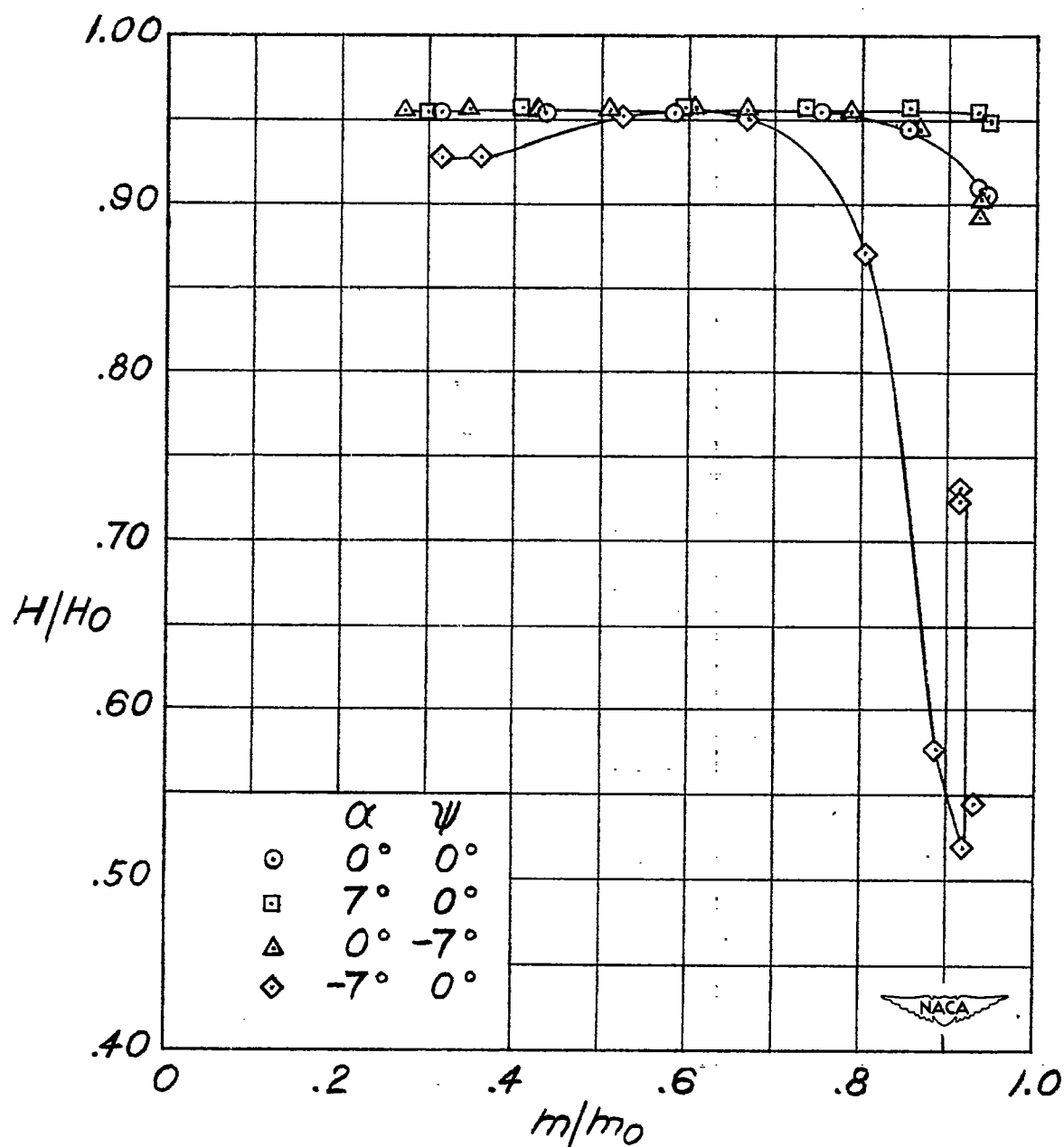
(a) Average total-pressure recovery at the inlet.
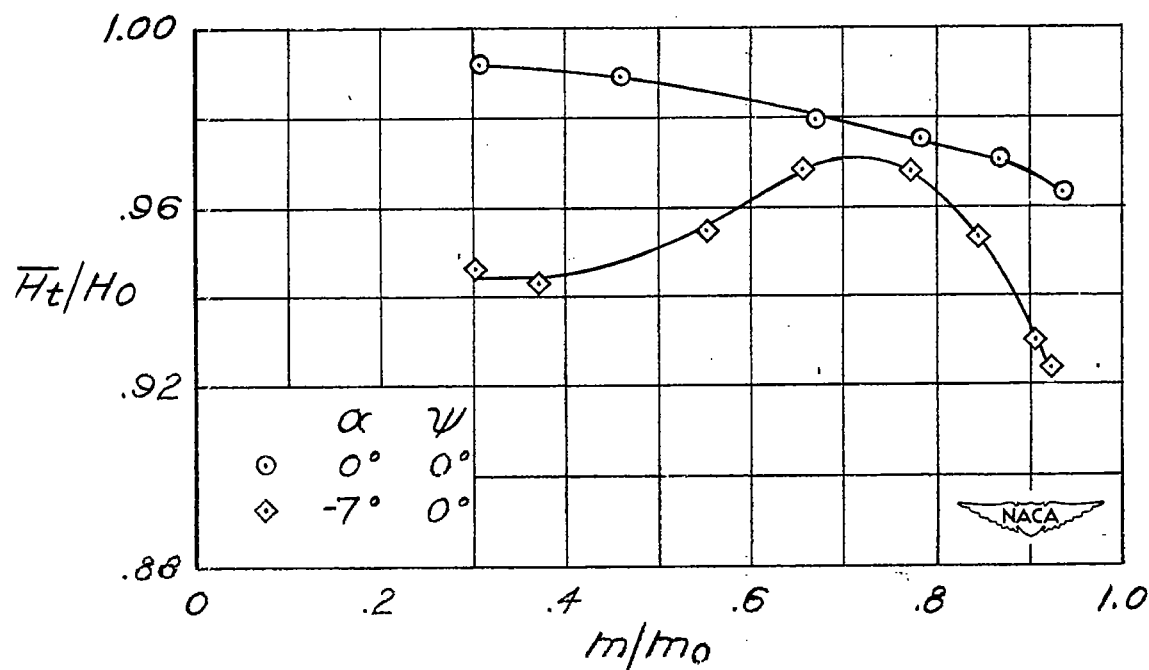
(b) Average total-pressure recovery at the throat.

Figure 9.- Average total-pressure recoveries as a function of mass-flow
ratio with the pointed nose installed.

(a) $\dfrac{m}{m_O}$ = 0.93.

(b) $\dfrac{m}{m_O}$ = 0.88.
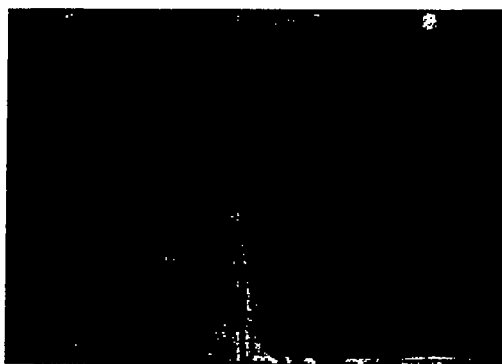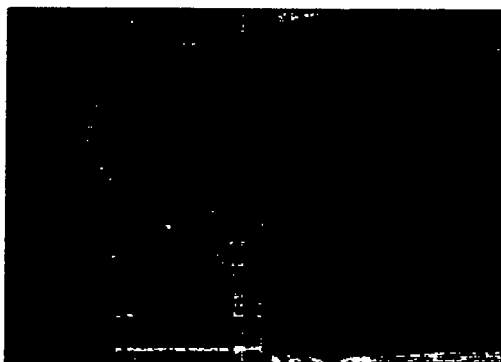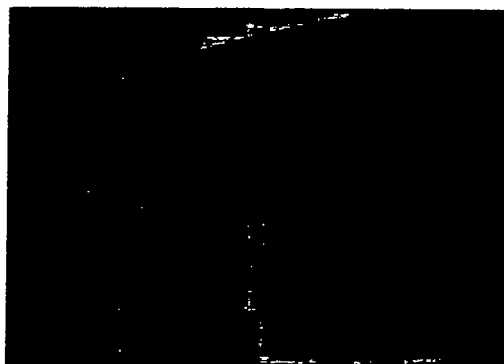
(c) $\dfrac{m}{m_O}$ = 0.30.

L-70838

Figure 10.- Shadowgraphs of the flow with the 1.5-inch-radius nose. α = 0°;
ψ = 0°.

(a) $\frac{m}{m_O} = 0.92.$

(b) $\frac{m}{m_O} = 0.42.$

L-70839

Figure 11.- Shadowgraphs of the flow with the 1.5-inch-radius nose. $\alpha = 7^O$;
$\psi = 0^O$.
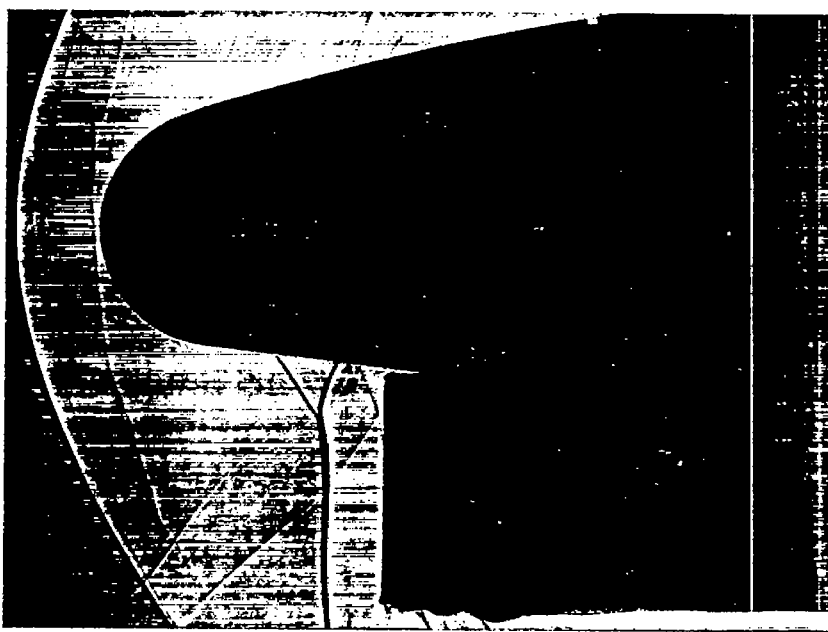
Figure 12.- Shadowgraph of the flow with the 1.5-inch-radius nose. $\frac{m}{m_0} = 0.90$; $\alpha = 0°$; $\psi = -7°$.
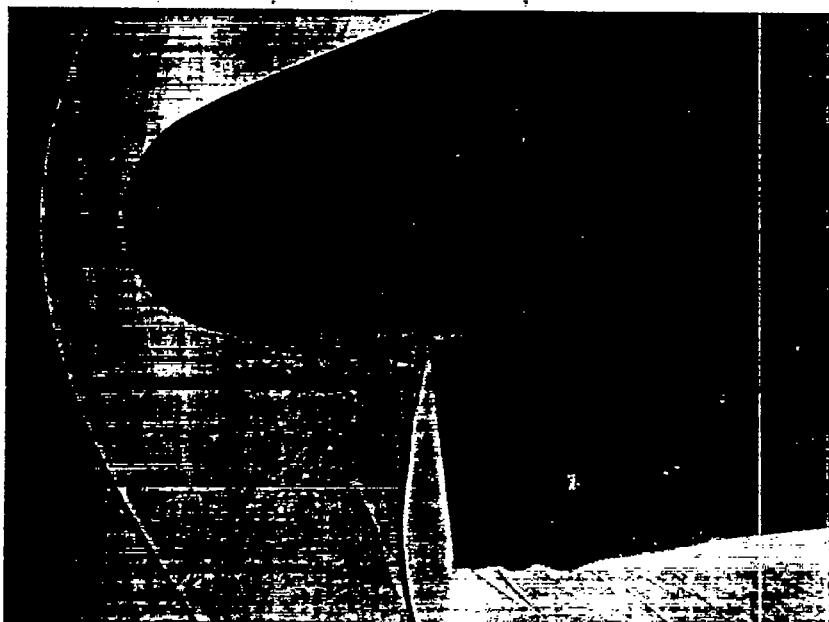
L-70840

Figure 13.- Shadowgraph of the flow with the 1.5-inch-radius nose. $\frac{m}{m_0} = 0.85$; $\alpha = -7°$; $\psi = 0°$.
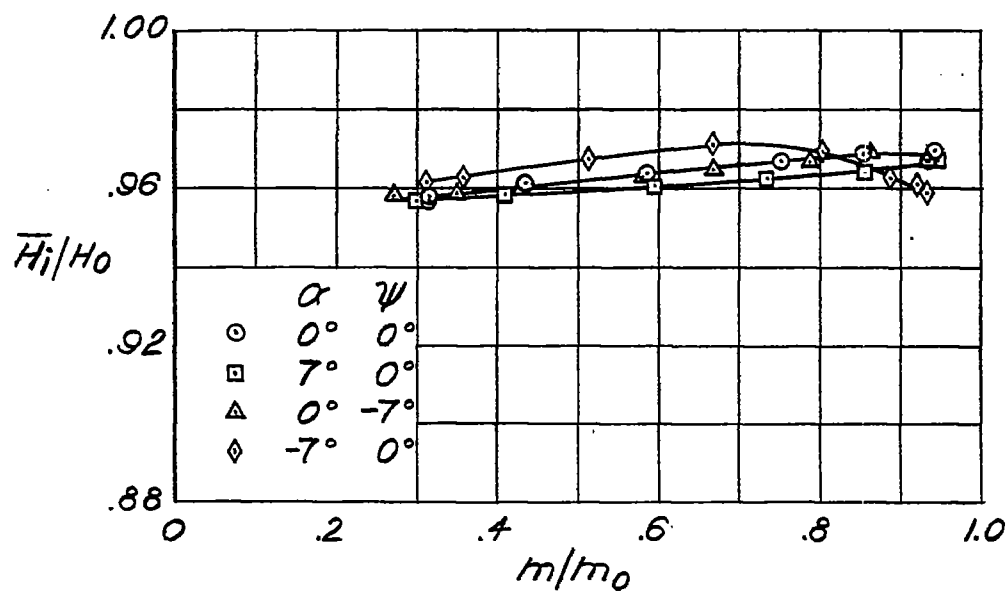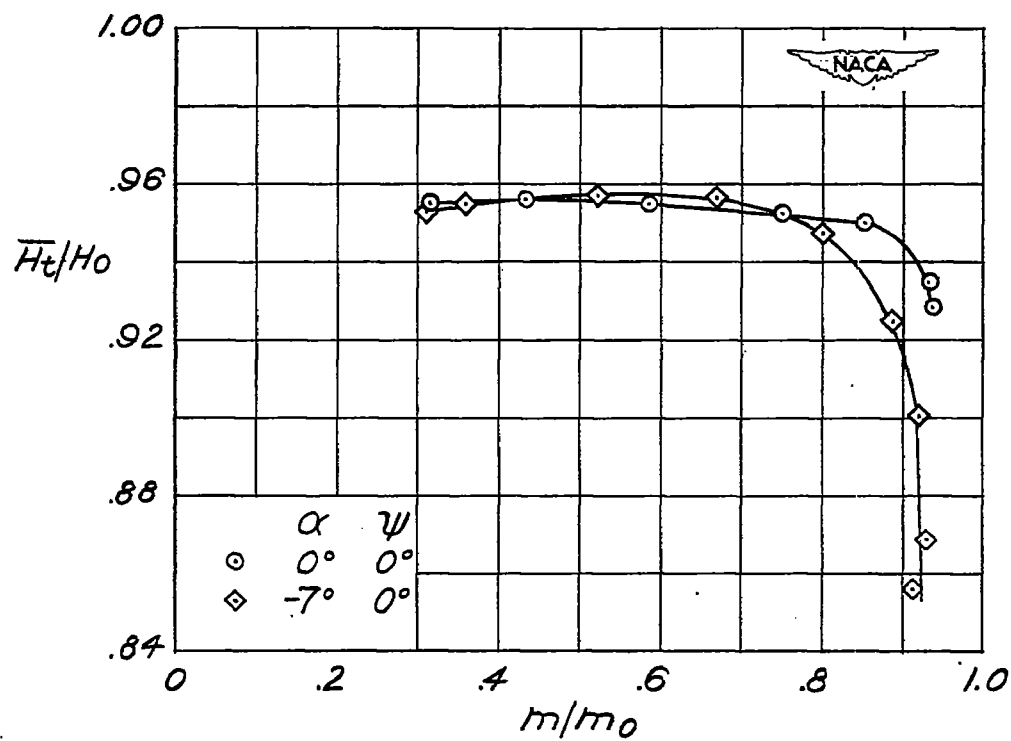
L-70841
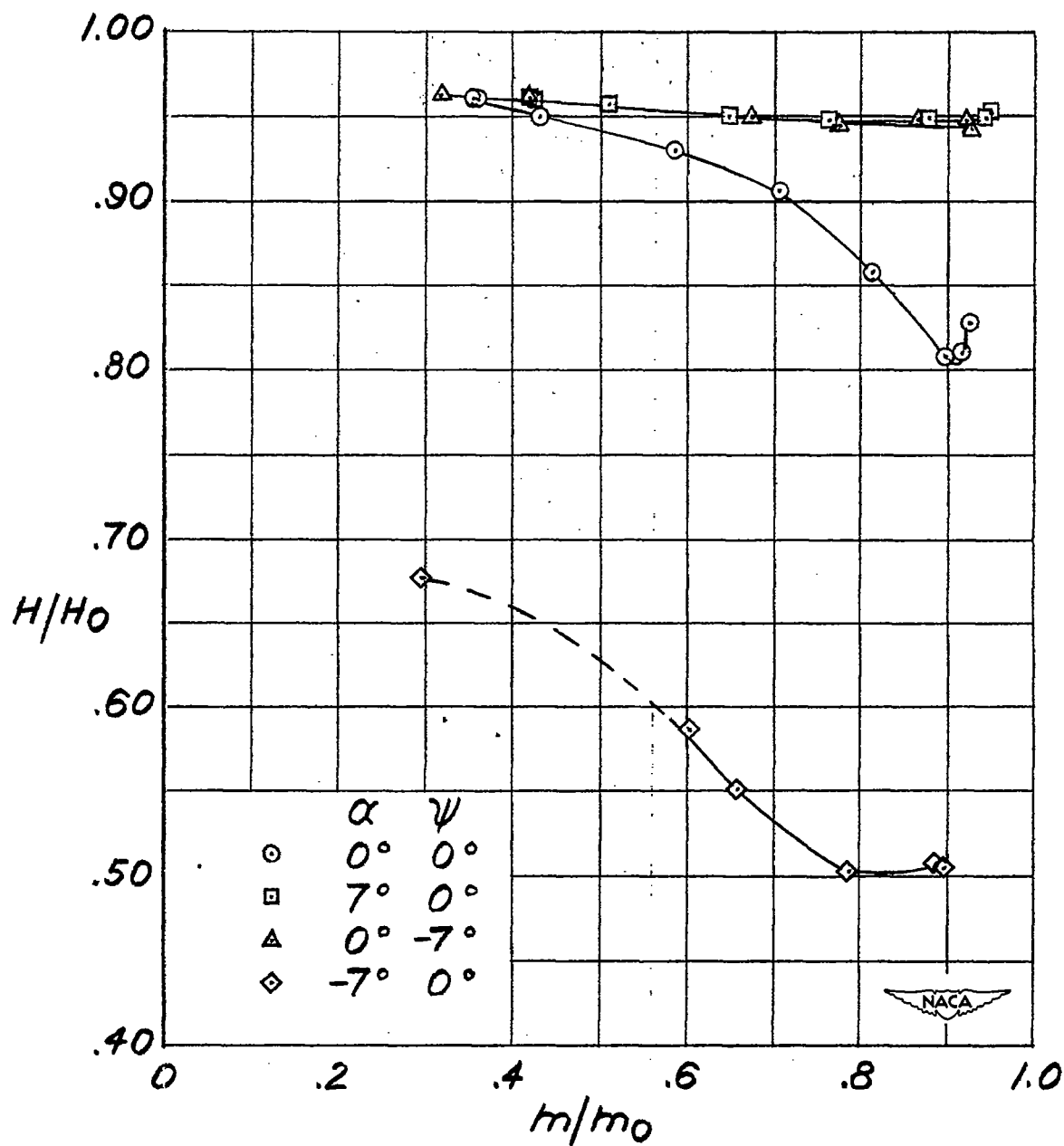
Figure 14.- Total-pressure recovery of inlet tube A with the 1.5-inch-radius nose installed.
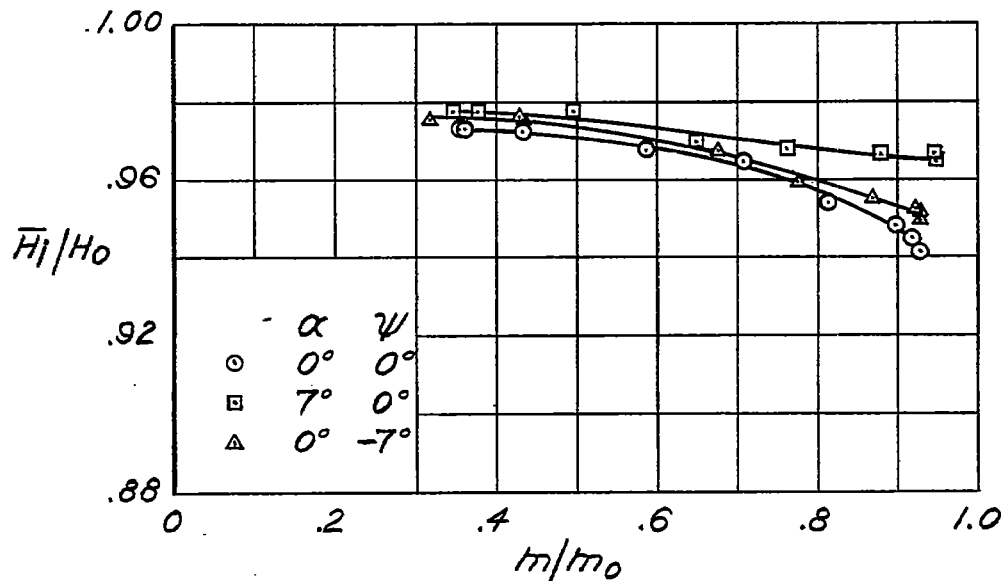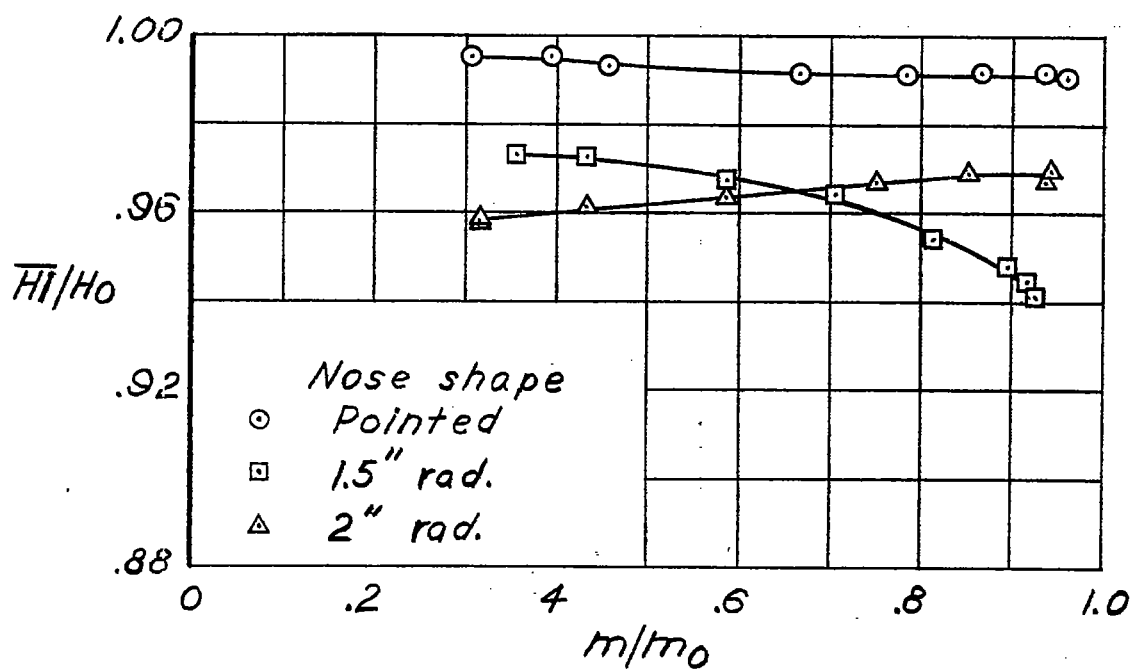
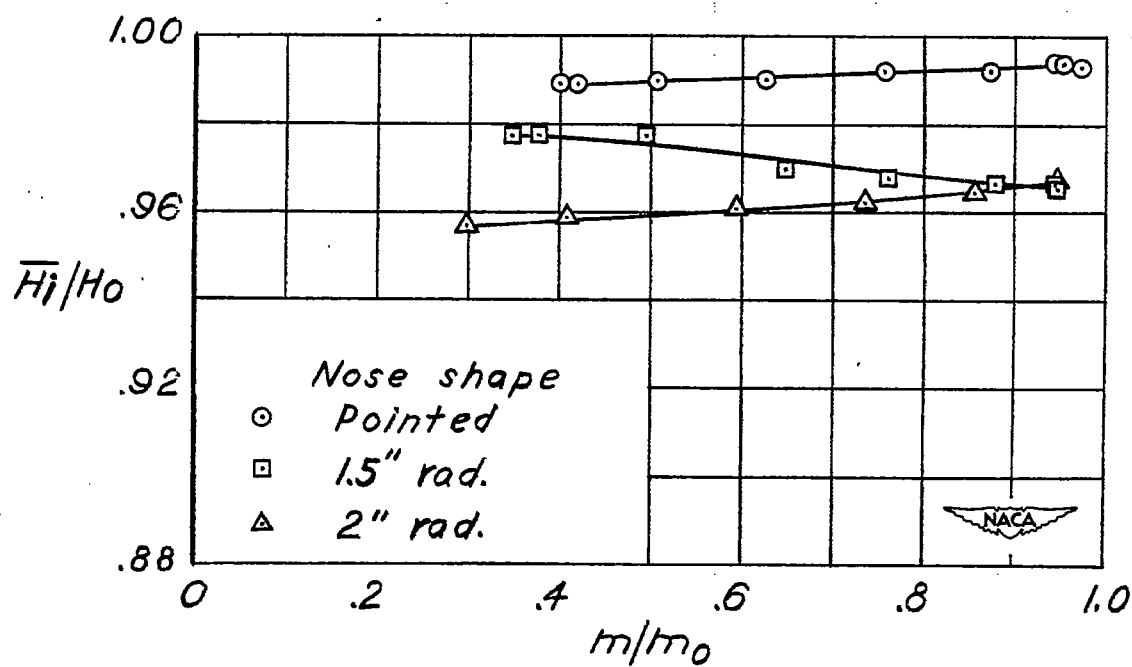(a) Average total-pressure recovery at the inlet.
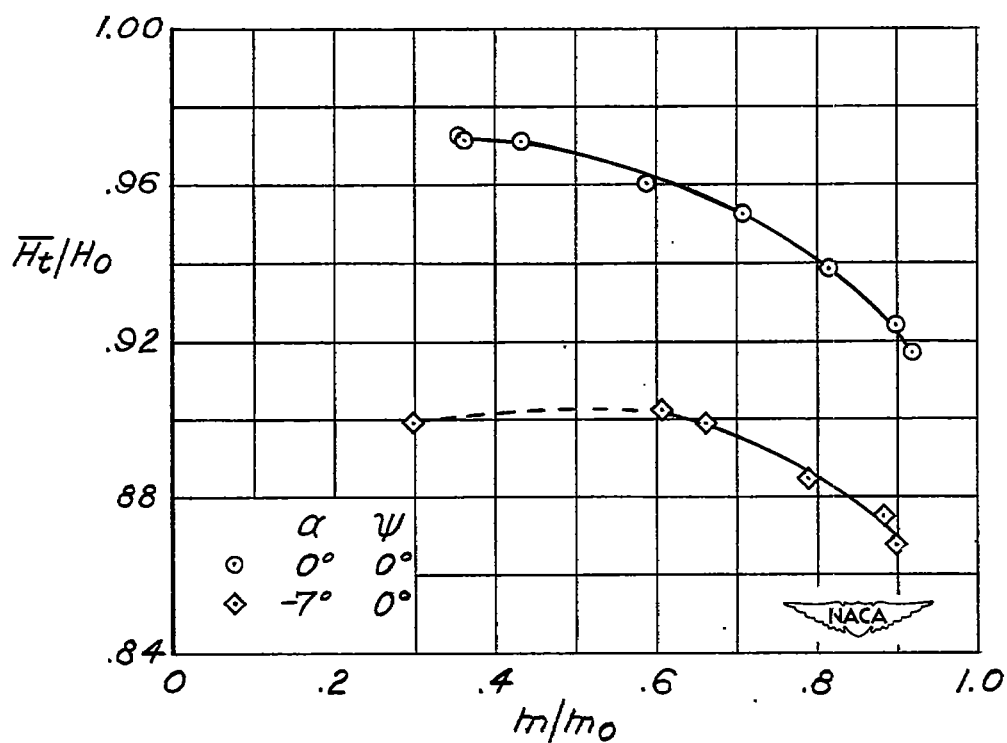
(b) Average total-pressure recovery at the throat.

Figure 15.- Average total-pressure recoveries as a function of mass-flow ratio with the 1.5-inch-radius nose installed.

CONFIDENTIAL

(a) $\dfrac{m}{m_O} = 0.94$.

(b) $\dfrac{m}{m_O} = 0.78$.

(c) $\dfrac{m}{m_O} = 0.31$.

L-70842

Figure 16.- Shadowgraphs of the flow with the 2-inch-radius nose. $\alpha = 0°$;
$\psi = 0°$

(a) $\frac{m}{m_0} = 0.94.$

(b) $\frac{m}{m_0} = 0.30.$

Figure 17.- Shadowgraphs of the flow with the 2-inch-radius nose. $\alpha = 7^\circ$; $\psi = 0^\circ$.

L-70843

(a) $\frac{m}{m_0} = 0.92.$

(b) $\frac{m}{m_0} = 0.64.$

Figure 18.- Shadowgraphs of the flow with the 2-inch-radius nose. $\alpha = -7^\circ$; $\psi = 0^\circ$.

L-70844

Figure 19.- Total-pressure recovery of inlet tube A with the 2-inch-radius nose installed.

(a) Average total-pressure recovery at the inlet.

(b) Average total-pressure recovery at the throat.

Figure 20.- Average total-pressure recoveries as a function of mass-flow
ratio with the 2-inch-radius nose installed.

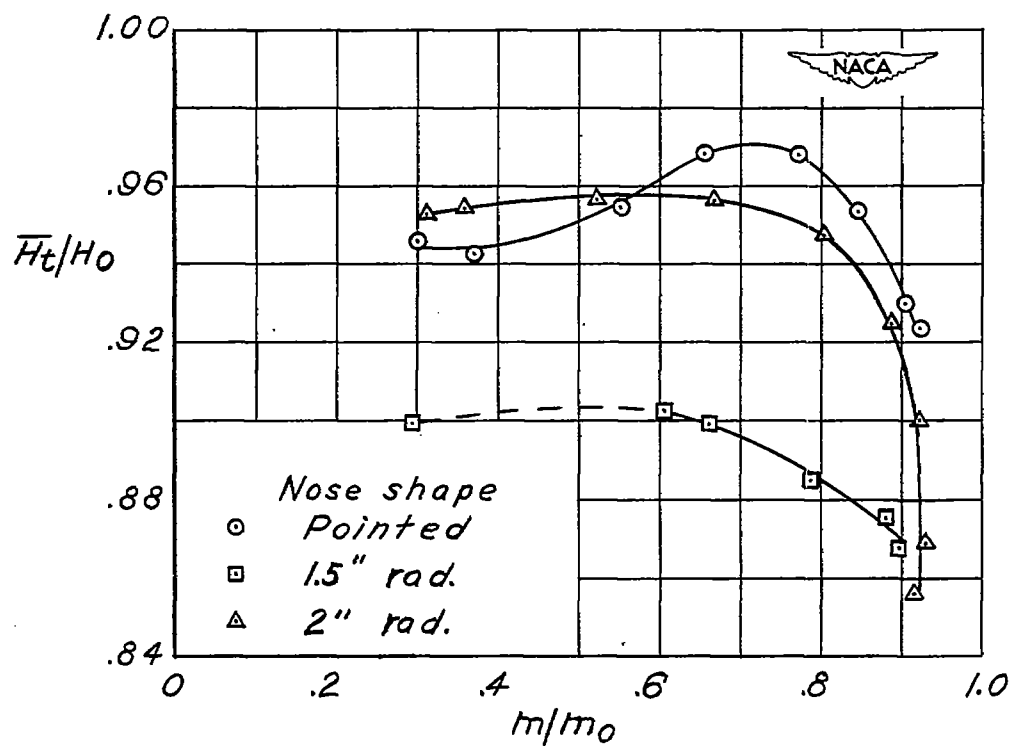(a) Average total-pressure recovery at the inlet. $\alpha = 0°$; $\psi = 0°$.

(b) Average total-pressure recovery at the inlet. $\alpha = 7°$; $\psi = 0°$.

Figure 21.- Comparison of the average total-pressure recoveries with the three nose shapes at different angles of attack and yaw.
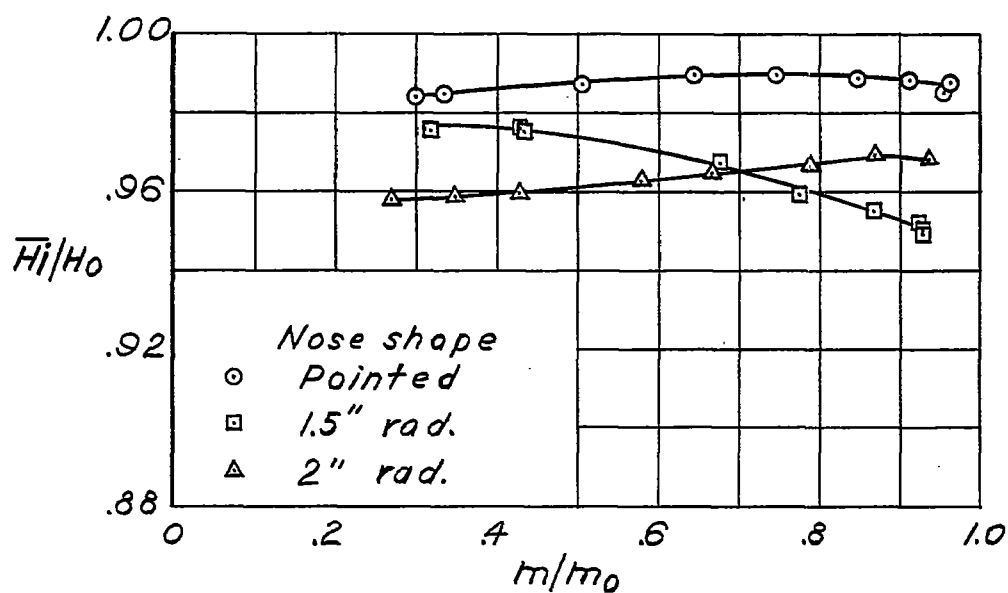
(c) Average total-pressure recovery at the inlet. $a = 0°$; $\psi = -7°$.

(d) Average total-pressure recovery at the throat. $a = -7°$; $\psi = 0°$.

Figure 21.- Concluded.
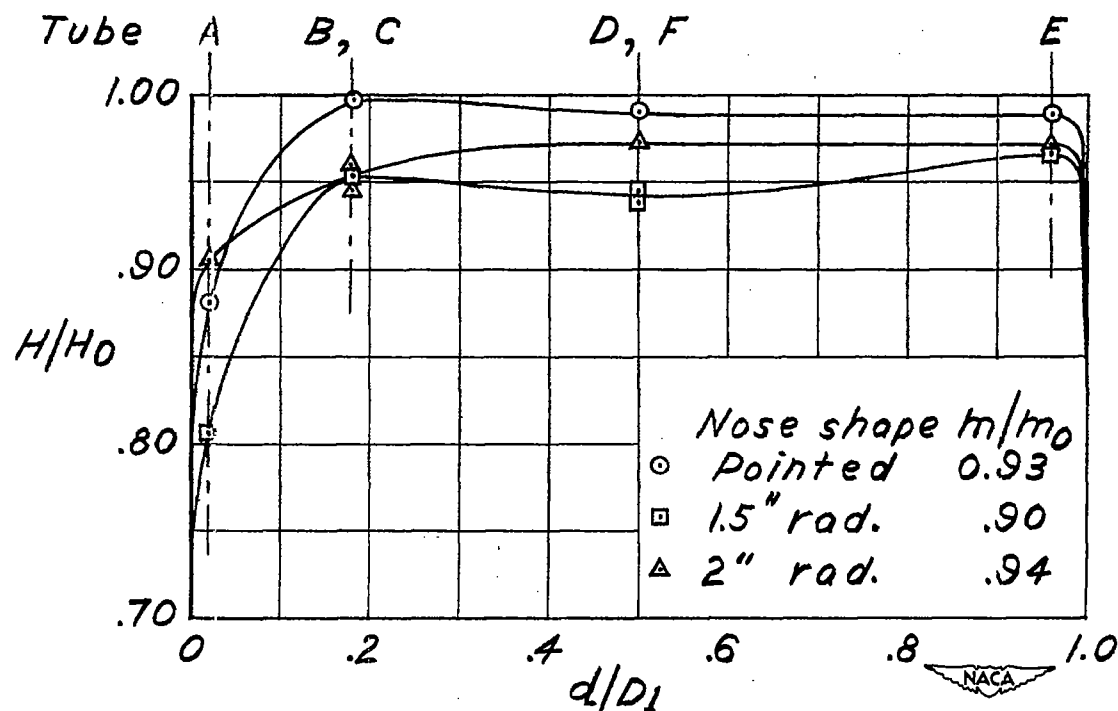
Figure 22.- Typical total-pressure distributions at the inlet for the three nose shapes at high mass-flow ratios. $\alpha = 0°$; $\psi = 0°$.
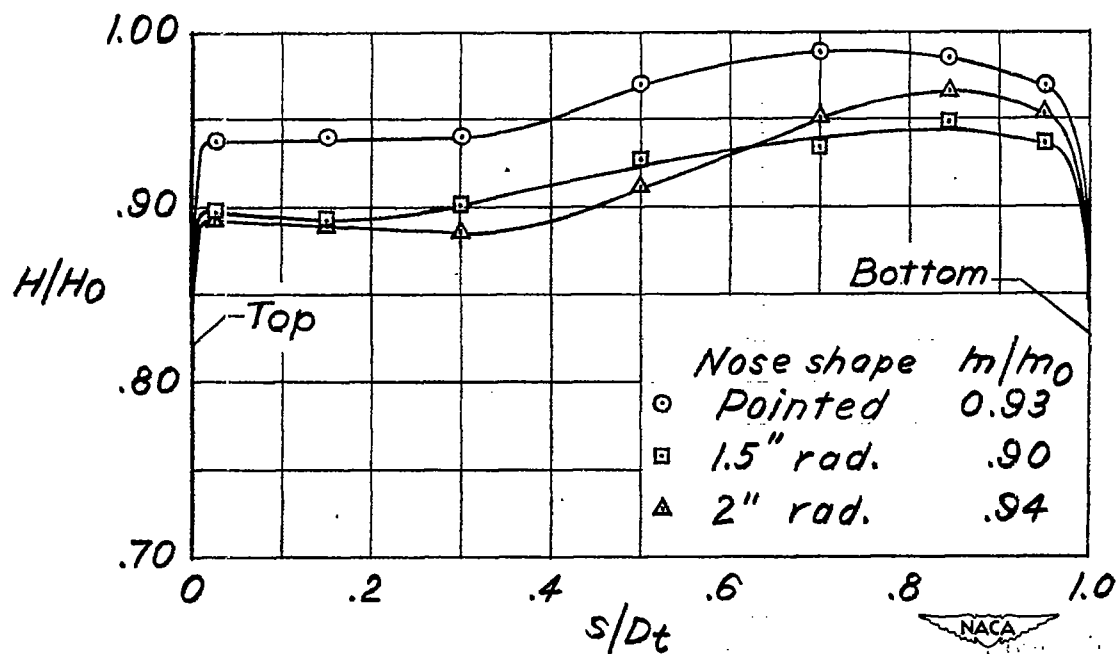

Figure 23.- Typical total-pressure distributions at the throat for the three nose shapes at high mass-flow ratios. $\alpha = 0°$; $\psi = 0°$.
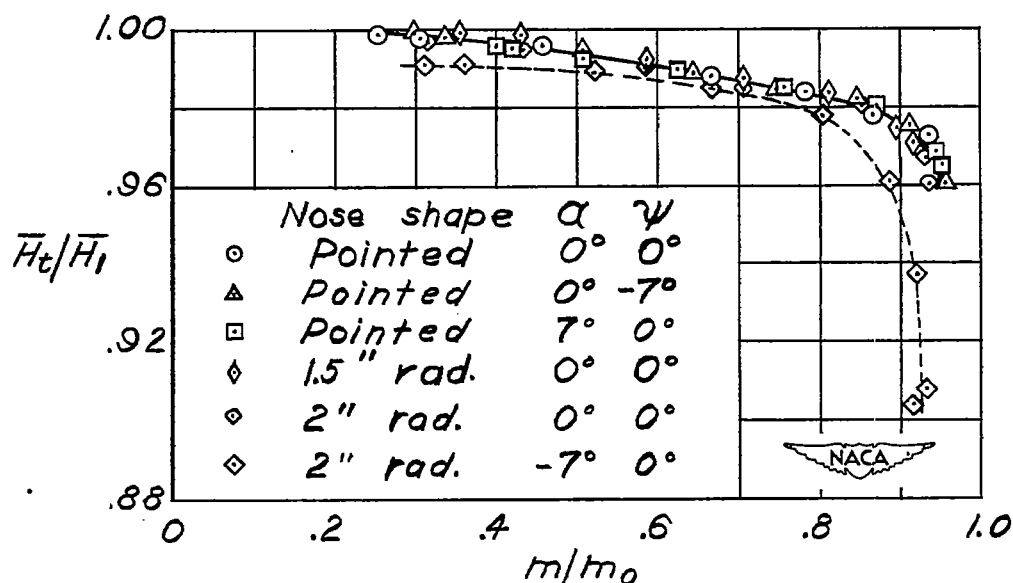
Figure 24.- Average total-pressure recovery of the diffuser-bend combination as a function of mass-flow ratio.
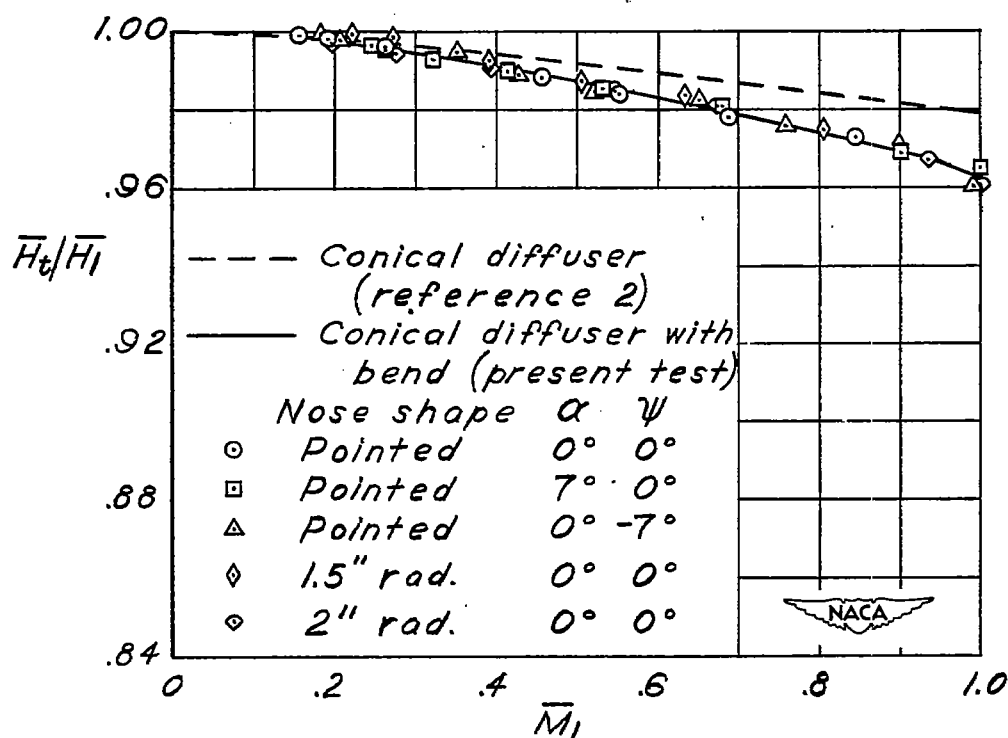

Figure 25.- Average total-pressure recovery of the diffuser-bend combination as a function of average Mach number at the entrance to the diffuser.